Sensors & Actuators: B. Chemical 418 (2024) 136367

Contents lists available at ScienceDirect

Sensors and Actuators: B. Chemical

journal homepage: www.elsevier.com/locate/snb

Rational design of an activatable dual-color fluorogenic probe for revealing the interaction of adenosine-5′-triphosphate and peroxynitrite in pyroptosis associated with acute kidney injury

Yuxia Zou [a,b,1], Tingting Duan [a,1], Yan Wang [b], Qing Ye [b,*], Yiying Li [a], Xiaofeng Wang [a], Xuan Liu [a], Xuejun Zhou [a], Fabiao Yu [a,c,**], Heng Liu [a,c,**]

[a] Key Laboratory of Emergency and Trauma of Ministry of Education, Department of Otolaryngology, Head and Neck Surgery, The First Affiliated Hospital of Hainan Medical University, Hainan Medical University, Haikou 571199, China
[b] Shengli Clinical Medical College of Fujian Medical University, Department of Otolaryngology, Head and Neck Surgery, Fujian Provincial Hospital, Fuzhou 350001, China
[c] Key Laboratory of Hainan Trauma and Disaster Rescue, Engineering Research Center for Hainan Bio-Smart Materials and Bio-Medical Devices, College of Emergency and Trauma, Hainan Medical University, Haikou 571199, China

ARTICLE INFO

Keywords:
Adenosine-5′-triphosphate
Peroxynitrite
Dual-color
Pyroptosis
Acute kidney injury

ABSTRACT

ATP and $ONOO^-$ play unique roles in various biological events and exhibit notable interactions. To date, there is no available chemical tool for investigating the correlation between ATP and $ONOO^-$ concentrations in pyroptosis associated with acute kidney injury (AKI). Herein, we designed a novel dual-color near-infrared fluorescent (NIRF) probe P2 for simultaneous visualization of ATP and $ONOO^-$ both *in vitro* and *in vivo*. Unlike previously reported single-site fluorescent probes, P2 enabled concurrent imaging of ATP and $ONOO^-$ in two distinct fluorescence channels, with emission wavelengths centered at 585 and 690 nm, which greatly reduced spectral cross-talk. Employing a HK-2 pyroptosis model, a significant interaction between ATP and $ONOO^-$ was unveiled. Elevated $ONOO^-$ production was found to correlate with decreased ATP levels; conversely, an increase in ATP levels was associated with rapid $ONOO^-$ scavenging. Remarkably, P2 allowed the assessment of cellular hypoxia by monitoring ATP and $ONOO^-$ concentrations. The commercial $ONOO^-$-scavenger uric acid showcased a protective effect on HK-2 cells via inhibition of the cellular pyroptosis pathway. Furthermore, P2 was successfully employed for imaging of ATP and $ONOO^-$ in the AKI mice model. Our findings confirmed that renal ischemia-reperfusion triggered a rise in $ONOO^-$ levels, concurrent with a decline in ATP levels. Surprisingly, the cells exhibited a compensatory recovery of ATP levels as the reperfusion time was prolonged. These results suggested the newly devised P2, as a pivotal chemical tool for the simultaneous monitoring of ATP and $ONOO^-$, might open new avenues for disease diagnosis and treatment.

1. Introduction

Adenosine-5′-triphosphate (ATP), primarily synthesized through cellular respiration, stands as a vital energy source for organisms. Disruption of ATP homeostasis is closely related to oxidative stress, which arises from the production of reactive oxygen species (ROS) [1–3]. Notably, peroxynitrite ($ONOO^-$), an important ROS, is produced in response to stressful inflammation *in vivo*, further exacerbating the inflammatory response and causing cellular and tissue damage [4,5]. In recent years, the emergence of pyroptosis, a novel form of programmed cell death observed in inflammatory cells, has attracted considerable attention. Often referred to as cellular inflammatory necrosis, pyroptosis triggers the activation of multiple caspases through inflammatory vesicles, leading to the cleavage of gasdermin family members, including GSDMD, culminating in cell death [6,7]. This process plays a significant role in inflammatory-related diseases, such as atherosclerotic,

* Corresponding author.
** Corresponding authors at: Key Laboratory of Emergency and Trauma of Ministry of Education, Department of Otolaryngology, Head and Neck Surgery, The First Affiliated Hospital of Hainan Medical University, Hainan Medical University, Haikou 571199, China.
E-mail addresses: 1158113213@qq.com (Q. Ye), yufabiao@hainmc.edu.cn (F. Yu), liuheng11b@hubu.edu.cn (H. Liu).
[1] These two authors contributed equally to this work (Y. X. Zou and T. T. Duan).

https://doi.org/10.1016/j.snb.2024.136367
Received 11 April 2024; Received in revised form 17 June 2024; Accepted 24 July 2024
Available online 25 July 2024

neurological, and urological diseases [8–10]. Pyroptosis can be initiated by various pathological conditions, including oxidative stress. ATP is a key molecule in the non-classical pyroptosis pathway, and intracellular ATP levels tend to decrease during pyroptosis, which may be linked to cellular energy metabolism and oxidative stress [11–13]. As such, investigating changes in ATP and $ONOO^-$ levels in pyroptosis is essential to elucidate their mechanisms of action and relationships with various diseases.

The involvement of pyroptosis in the progression of acute kidney injury (AKI) has been reported [14–16]. AKI encompasses a group of clinical syndromes characterized by a sudden and profound deterioration in renal function, resulting in increased serum creatinine, decreased urine output, vascular dysfunction, intense inflammatory response, and tubular epithelial cell injury [17,18]. Early detection and elimination of risk factors for acute tubular necrosis are crucial in preventing AKI, considering its diverse etiologies, with acute ischemia being one of the most common. Renal ischemia can damage vascular endothelial cells through an inflammatory response or inflammatory mediators produced by renal tubular cells, making ischemic AKI a stress-inflammatory disease. The release of superoxide anion and nitric oxide from glomerular capillary endothelial cells upregulates the levels of $ONOO^-$ through diffusion reactions in AKI. $ONOO^-$'s potent oxidative properties can induce apoptosis and necrosis of renal tubular epithelial cells and activate inflammatory reactions, leading to oxidative damage of the glomerular filtration membrane [19]. Normal renal cells require high levels of ATP to maintain physiological functions. However, in the context of AKI, the concentration of ATP decreases significantly due to the ischemic and hypoxic state of renal tissues, affecting intracellular metabolism and functions [20–22]. Previous studies have shown that $ONOO^-$ decreases ATPase activity, inhibits ATP synthesis, and ultimately downregulates ATP levels in renal tissue [23,24]. Consequently, ATP and $ONOO^-$ are implicated in the onset and progression of AKI, and a detailed study of their interaction mechanisms will be beneficial for the early diagnosis and treatment of AKI [25].

For the past few years, numerous single-site near-infrared fluorescent (NIRF) probes have been developed for the specific monitoring of ATP or $ONOO^-$ levels in cells or *in vivo* [26–43]. Nevertheless, NIRF probes capable of imaging both ATP and $ONOO^-$ with minimal emission spectra crosstalk are rare [44]. Addressing this challenge, we engineered two structurally novel dual-color readout NIRF probes by integrating rhodamine and methylene blue into a molecular backbone via diethylenetriamine or 1-(2-aminoethyl) piperazine linker. Among them, P2 offered superior anti-interference performance. Even in the simultaneous presence of ATP and $ONOO^-$, P2 was able to differentiate between ATP and $ONOO^-$ with minimal spectral overlap in two distinct fluorescence channels, which greatly reduced the output of false-positive fluorescence signals in the detection process. The reaction of ATP or $ONOO^-$ with P2 triggered rhodamine ring-opening or methylene blue deformylation, which correspondingly showed intense fluorescence signals at 585 and 690 nm. This spectral change provided an intuitive and sensitive means of detecting ATP and $ONOO^-$ in cells and mice. Leveraging P2, it was not only possible to distinguish normal from cancer cells but also verified the existence of intracellular ATP and $ONOO^-$ interactions. Importantly, through dynamic monitoring of ATP and $ONOO^-$ level fluctuations in pyroptosis, uric acid (UA) was found to be a potential inhibitor of pyroptosis. For the first time, P2 was employed to demonstrate a negative correlation between the expression levels of ATP and $ONOO^-$ in AKI, characterized by increased $ONOO^-$ levels and decreased ATP levels. Overall, this innovative dual-color activated NIRF probe P2 afforded an indispensable chemical tool for elucidating the complex roles of ATP and $ONOO^-$ in pyroptosis associated with AKI.

2. Experimental section

2.1. Materials and apparatus

The apparatus, materials, fluorescence analysis, analytes solution preparation, cytotoxicity, cellular model, and in vivo imaging in the AKI mice model were listed in the Supporting information.

2.2. Synthesis and characterization of P1

Sodium carbonate (318 mg, 3.0 mmol) was added to a stirred solution of 2-(2-((2-aminoethyl)amino)ethyl)-3′,6′-bis(diethylamino)spiro[isoindoline-1,9′-xanthen]-3-one (527 mg, 1.0 mmol) and MB-Cl (347 mg, 1.0 mmol) in CH_2Cl_2. The reaction mixture was stirred at room temperature overnight. After the reaction was stopped, the solvent was removed under reduced pressure. The crude products were directly purified on a silica gel column (200–300 mesh) using CH_2Cl_2/CH_3OH (30/1) to obtain the desired compound P1 as a purple solid in 35 % isolated yield (293 mg). ^1H NMR (400 MHz, $CDCl_3$): 7.89–7.87 (m, 1 H), 7.45–7.43 (m, 2 H), 7.31 (d, $J = 8.6$ Hz, 2 H), 7.10–7.08 (m, 1 H), 6.64 (d, $J = 2.7$ Hz, 2 H), 6.57 (dd, $J = 8.8$, 2.8 Hz, 2 H), 6.41 (d, $J = 8.8$ Hz, 2 H), 6.37 (d, $J = 2.6$ Hz, 2 H), 6.23 (dd, $J = 8.9$, 2.6 Hz, 2 H), 5.43 (s, 1 H), 3.31 (q, $J = 7.1$ Hz, 8 H), 3.23–3.11 (m, 4 H), 2.89 (s, 12 H), 2.43–2.34 (m, 4 H), 2.03–1.98 (m, 1 H), 1.14 (d, $J = 7.0$ Hz, 12 H); ^{13}C NMR (100 MHz, $CDCl_3$): 168.63, 156.02, 153.51, 153.26, 148.82, 148.78, 132.92, 132.46, 131.01, 128.68, 128.49, 128.03, 127.20, 123.83, 122.73, 111.39, 110.84, 108.04, 105.21, 97.60, 65.12, 48.20, 47.60, 44.31, 40.74, 40.18, 12.55. HRMS *m/z*: $C_{51}H_{60}N_8O_3S$ $[M]^+$ calcd for 838.4353 found 838.4391.

2.3. Synthesis and characterization of P2

Sodium carbonate (318 mg, 3.0 mmol) was added to a stirred solution of Rh-N (553 mg, 1.0 mmol) and MB-Cl (347 mg, 1.0 mmol) in CH_2Cl_2. The reaction mixture was stirred at room temperature overnight. After the reaction was stopped, the solvent was removed under reduced pressure. The crude products were directly purified on a silica gel column (200–300 mesh) using CH_2Cl_2/CH_3OH (30/1) to obtain the desired compound P2 as a purple solid in 67 % isolated yield (583 mg). ^1H NMR (400 MHz, $CDCl_3$): 7.86–7.84 (m, 1 H), 7.49 (d, $J = 9.0$ Hz, 2 H), 7.42 – 7.38 (m, 2 H), 7.06–7.04 (m, 1 H), 6.62 (d, $J = 2.8$ Hz, 2 H), 6.55 (dd, $J = 8.9$, 2.8 Hz, 2 H), 6.40 (d, $J = 8.8$ Hz, 2 H), 6.34 (d, $J = 2.6$ Hz, 2 H), 6.22 (dd, $J = 8.8$, 2.5 Hz, 2 H), 3.31 (q, $J = 7.1$ Hz, 8 H), 3.19 (t, $J = 7.3$ Hz, 2 H), 3.13–3.10 (m, 4 H), 2.89 (s, 12 H), 2.09–2.07 (m, 4 H), 2.01 (t, $J = 7.4$ Hz, 2 H), 1.14 (t, $J = 7.0$ Hz, 12 H); ^{13}C NMR (100 MHz, $CDCl_3$): 167.91, 158.18, 153.54, 153.21, 148.63, 148.11, 132.21, 131.56, 131.16, 131.09, 128.98, 127.87, 123.90, 123.68, 122.61, 111.65, 110.91, 107.89, 105.56, 97.60, 64.68, 55.41, 52.29, 45.83, 44.33, 40.81, 12.56. HRMS *m/z*: $C_{51}H_{60}N_8O_3S$ $[M + H]^+$ calcd for 865.4587 found 865.4534.

2.4. Cell culture and Imaging

CNE1, NP69, 5–8 F, CNE2, and HK-2 cells were cultured as normal, and the cells were inoculated into laser-confocal specialized culture dishes after they had grown to 90 %. The cells were cultured at a temperature of 37°C containing 95 % air and 5 % CO_2 until the cells adhered to the wall. The cells were stained with 20 μM P2 and imaged. Fluorescent images were acquired on a Zeiss LSM 510 META laser confocal microscope with an objective lens (× 60). Ch1 channels (ATP, λ_{ex} = 530 nm) were collected from 540 nm to 620 nm; Ch2 channels ($ONOO^-$, λ_{ex} = 630 nm) were collected from 650 nm to 740 nm.

3. Results and discussion

3.1. Design principles for the P1 and P2

Rhodamine and methylene blue, two popular dyes with outstanding optical properties and biocompatibility, have been widely employed as core structures for the construction of activatable fluorescent probes. Although dual-reaction site fluorescent probes based on rhodamine have been reported, the challenge of selecting two suitable dyes to minimize excitation and emission overlap for enhancing signal-to-noise ratios in bioimaging applications was still an urgent issue [45–48]. In this design, P1 and P2 were composed of three components: a rhodamine unit, a methylene blue unit, and a linker unit (Scheme 1). A detailed synthesis of P1 and P2 was outlined in Figures S1 and S5, respectively. The molecular structures of P1 and P2 were confirmed by ^{1}H NMR, ^{13}C NMR, and MS (Figure S2-S4, S6-S8). P1 and P2 fluoresce weakly at 585 and 690 nm due to the closed ring of rhodamine and the de-aromatization of methylene blue. The addition of ATP induced strong fluorescence from rhodamine ring-opening, which was attributed to the hydrogen bonding of the phosphate of ATP with the amino group and the π-π interaction of the adenine of ATP with rhodamine. Exposure to $ONOO^-$ triggered the release of methylene blue via oxidative deformylation, yielding a robust fluorescence at 690 nm. To verify the sensing mechanism, the reaction of ATP or $ONOO^-$ with P2 was carried out. HRMS results revealed the presence of a major peak at *m/z* 1371.4430 assigned to the complex P2-ATP (Figure S9). Two dominant peaks at *m/z* 576.3358 and 284.1278 corresponded to the cleaved rhodamine derivative Rh-N and methylene blue (Figure S10).

3.2. In vitro spectral characterization of P1 and P2

With P1 and P2 in hand, UV–vis and fluorescence emission spectra were initially conducted. Both P1 and P2 presented new maximum absorption peaks at 565 or 668 nm after the addition of ATP or $ONOO^-$. At the same time, significant fluorescence enhancement at the emission wavelength of 585 or 690 nm under 530 or 630 nm excitation was observed (Fig. 1a-f). Given the complexity of the biological environment, particular attention was paid to potential spectral interferences during the detection of ATP and $ONOO^-$ that could affect the accuracy of the assay. Specifically, $ONOO^-$, ATP, ATP + $ONOO^-$ (ATP first, then $ONOO^-$), and $ONOO^-$ + ATP ($ONOO^-$ first, then ATP) were added to the solution of P2 to measure the fluorescence spectra. Notably, the addition of ATP, ATP + $ONOO^-$, and $ONOO^-$ + ATP all triggered noticeable fluorescence enhancement at 585 nm under 530 nm excitation, with no significant difference between the intensities (Fig. 1e). When $ONOO^-$ was added, the fluorescence change was almost imperceptible. Similarly, the addition of $ONOO^-$, ATP + $ONOO^-$, and $ONOO^-$ + ATP initiated sharp fluorescence changes at 690 nm under 630 nm excitation, whereas ATP alone gave a negligible fluorescence change (Fig. 1f). For P1, there were no significant differences in the fluorescence response in the presence of $ONOO^-$, ATP + $ONOO^-$, and $ONOO^-$ + ATP under 630 nm excitation (Fig. 1c). However, with the excitation of 530 nm, ATP + $ONOO^-$, and $ONOO^-$ + ATP exhibited markedly enhanced fluorescence intensity at 585 nm compared to ATP alone (Fig. 1b). This phenomenon indicated that $ONOO^-$ might interfere with the accurate measurement of ATP concentration in the detection system of P1. By comparing the changes in fluorescence between P1 and P2 across the two emission regions under various conditions, it was reasonable to believe that P2

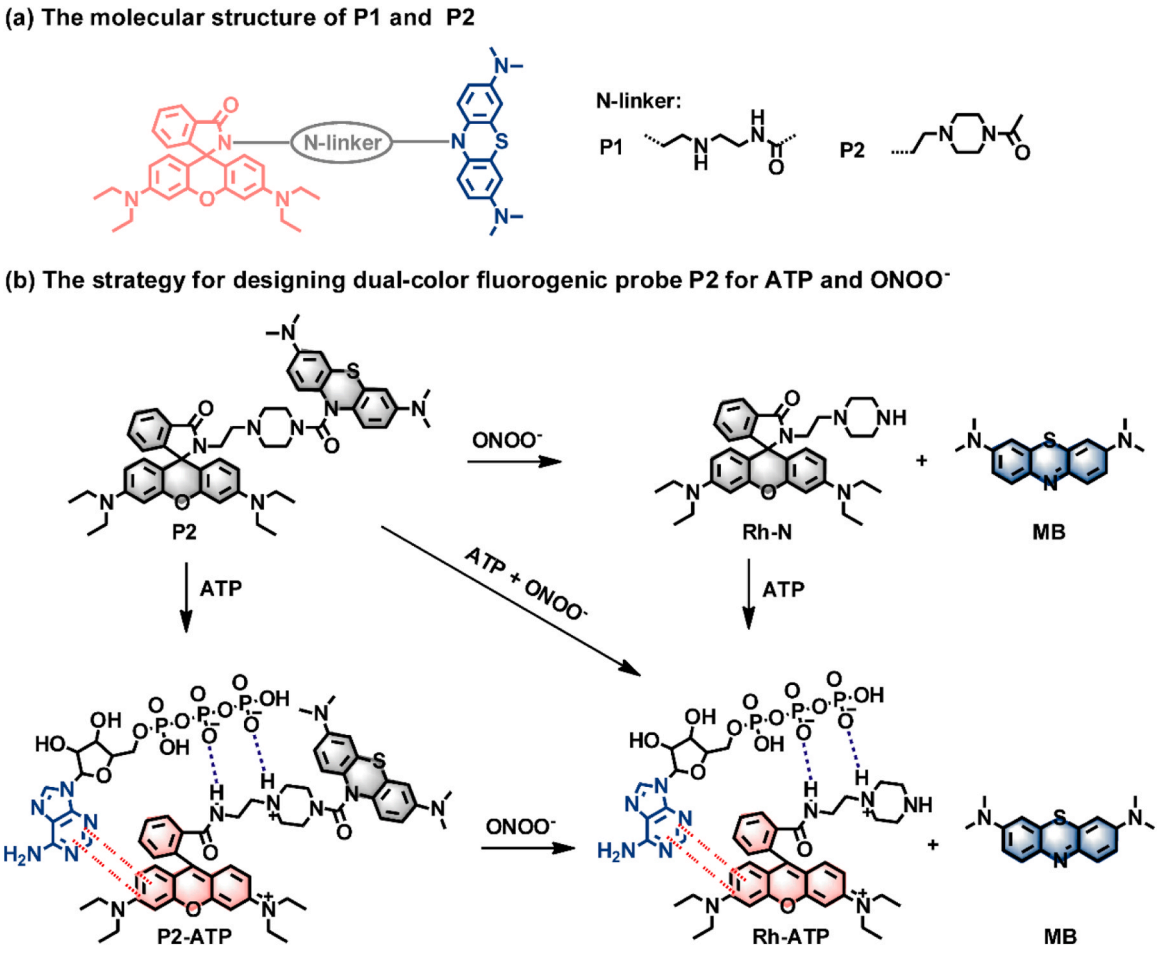

Scheme 1. (a) The molecular structure of P1 and P2. (b) The strategy for designing dual-color fluorogenic probe P2 for ATP and $ONOO^-$.

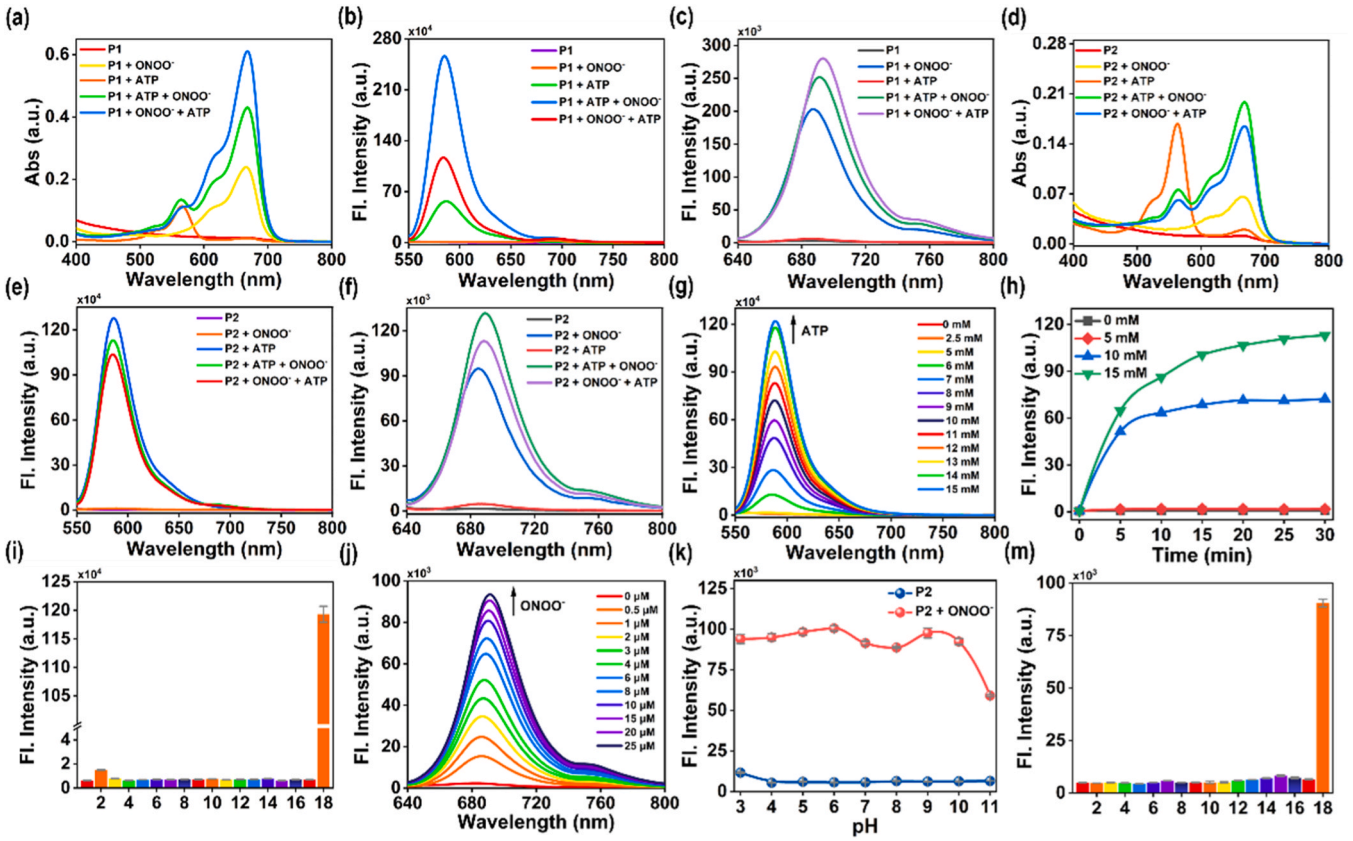

Fig. 1. Spectral characterization of 10 μM P1 or P2. (a-f) UV–vis and fluorescence spectra of P1 or P2 in the absence or presence of $ONOO^-$ (25 μM), ATP (15 mM), 15 mM ATP + 25 μM $ONOO^-$, 25 μM $ONOO^-$ + 15 mM ATP. (g) Fluorescence responses of P2 to increase concentrations of ATP from 0 to 15 mM. (h) Time-dependent fluorescence intensity of P2 in the presence of ATP (0, 5, 10, 15 mM). (i) Fluorescence enhancement at 585 nm of P2 upon treatment with different potential interfering species: 1) blank; 2) ADP (10 mM); 3) AMP (10 mM); 4) $H_2PO_4^-$ (500 μM); 5) HPO_4^{2-} (500 μM); 6) PO_4^{3-} (500 μM); 7) CO_3^{2-} (500 μM); 8) SO_4^{2-} (500 μM); 9) NO^{3-} (500 μM); 10) Cl^- (500 μM); 11) Na^+ (500 μM); 12) K^+ (500 μM); 13) Mg^{2+} (200 μM); 14) Ca^{2+} (200 μM); 15) Zn^{2+} (200 μM); 16) GSH (1 mM); 17) D-glucose (1 mM); 18) ATP (15 mM). (j) Fluorescence responses of P2 to increase concentrations of $ONOO^-$ from 0 to 25 μM. (k) pH influence on fluorescence intensity at 690 nm of P2 before and after the addition of 25 μM $ONOO^-$. (m) Fluorescence enhancement at 690 nm of P2 upon treatment with different potential interfering species: 1) blank; 2) $H_2PO_4^-$ (500 μM); 3) HPO_4^{2-} (500 μM); 4) PO_4^{3-} (500 μM); 5) CO_3^{2-} (500 μM); 6) SO_4^{2-} (500 μM); 7) NO^{3-} (500 μM); 8) Na^+ (500 μM); 9) K^+ (500 μM); 10) Mg^{2+} (200 μM); 11) Ca^{2+} (200 μM); 12) Zn^{2+} (200 μM); 13) GSH (1 mM); 14) H_2O_2 (100 μM); 15) ClO^- (100 μM); 16) ·OH (100 μM); 17) $^1O_2$ (100 μM); 18) $ONOO^-$ (25 μM). $\lambda_{ex/em}$ = 530/585 nm (ATP channel), $\lambda_{ex/em}$ = 630/690 nm ($ONOO^-$ channel).

could effectively eliminate the mutual interference of ATP and $ONOO^-$ in the detection process.

As depicted in Fig. 1g, the incremental addition of ATP (0–15 mM) resulted in a continuous increase in the emission intensity of P2. The fluorescence intensity of P2 at 585 nm showed an excellent linear relationship (R^2 = 0.99, linear equation: $F_{585\ nm}$ = 126,622.2 × [ATP] mM – 617,326.0) with the concentration of ATP (5–15 mM) (Figure S11, S12). The reaction kinetics between P2 and ATP was further investigated. When varying concentrations of ATP (0, 5, 10, 15 mM) were added to the solution of P2, the fluorescence intensity at 585 nm appeared to be enhanced to different degrees and reached a maximum within 20 min (Fig. 1h). This suggested that P2 was able to respond rapidly to ATP in the millimolar concentration range, consistent with physiological ATP levels in organisms. P2 itself exhibited minimal changes in fluorescence intensity at 585 nm in the pH range of 4.0–11.0. However, in the presence of ATP, fluorescence intensity presented a variable response within the pH range of 3.0–10.0, with a decay in an alkaline environment, possibly due to the weakened role of hydrogen bonding (Figure S13). The emission spectra changes of P2 before and after its reaction with $ONOO^-$ were explored. Upon the incremental addition of $ONOO^-$, the intensity of the emerging 690 nm emission peak was gradually enhanced (Fig. 1j). The fluorescence intensity at 690 nm displayed a good linear correlation (R^2 = 0.99, linear equation: $F_{690\ nm}$ = 8572.9 × [$ONOO^-$] μM + 15,841.5) with the $ONOO^-$ concentration (1–6 μM), and the limit of detection was found to be 138 nM (Figure S14, S15). Time-dependent fluorescence intensity changes of P2 on $ONOO^-$ were also examined. As can be seen from Figure S16, when $ONOO^-$ was added at 600 s, the fluorescence intensity increased sharply and reached a maximum within 50 s. The effect of pH on the fluorescence intensity of P2 at 690 nm was studied in the presence or absence of $ONOO^-$ (Fig. 1k). Over a pH range of 3.0 – 11.0, the changes in fluorescence intensity of P2 itself were negligible, while there were fluorescence responses in the presence of $ONOO^-$ in all cases. To evaluate selectivity, the fluorescence intensities of P2 at 585 and 690 nm in the presence of other bioactive molecules were recorded. Under 530 nm excitation, none of the bioactive molecules could induce changes in the fluorescence intensity of the detection system at 585 nm, except for ATP and ADP (Fig. 1i). Under 630 nm excitation, bioactive molecules elicited negligible fluorescence response of P2 at 690 nm, and only the addition of $ONOO^-$ produced a prominent fluorescence signal (Fig. 1m). These results confirmed that P2 enabled highly sensitive and specific detection of ATP and $ONOO^-$ in two relatively independent fluorescence emission ranges, providing a foundation for subsequent biological experiments.

3.3. Fluorescence imaging of ATP and $ONOO^-$ activity in cultured cells

In view of the excellent photophysical properties of P2 described above, we proceeded to investigate its potential for monitoring ATP and

$ONOO^-$ in cells. The CCK-8 assay played a crucial role in evaluating fluorescent probes in cellular and *in vivo* imaging studies. Therefore, the cytotoxicity of P2 was first assessed using the CCK-8 assay before bio-imaging (Figure S17). Upon exposure to varying concentrations of P2 from 0 to 1 mM for 24 h, the cell viability of human nasopharyngeal carcinoma cells (CNE1, 5–8 F, CNE2), human normal nasopharyngeal cells (NP69), and human kidney 2 cells (HK-2) were above 50 %, which indicated that P2 featured low cytotoxicity and good biocompatibility. Subsequently, CNE-1 and HK-2 cells were selected to verify the ability of P2 to image endogenous ATP and $ONOO^-$ at the cellular level. As depicted in Figure S18, faint fluorescent signals were immediately observed in the green (Ch 1, ATP) and red channels (Ch 2, $ONOO^-$) in CNE1 cells treated with P2. The fluorescence signal in both channels gradually intensified over 30 min. Similarly, HK-2 cells treated with P2 exhibited a weak fluorescent signal in Ch 1 (ATP) and a detectable signal in Ch 2 ($ONOO^-$) after 5 min (Figure S19). The fluorescence signals in both channels gradually increased with time from 0 to 30 min. However, the fluorescence signal in Ch 2 ($ONOO^-$) was overall weaker than that in CNE1 cells, indicating that the $ONOO^-$ concentration in HK-2 cells was lower than that of CNE1 cells. The imaging results of CNE1 and HK-2 cells demonstrated that P2 could track endogenous ATP and $ONOO^-$ in cells.

Afterward, the imaging of ATP and $ONOO^-$ interactions in cells with P2 was examined. In the control group, CNE1 cells stained with P2 for 20 min showed a robust green fluorescence signal in Ch 1 (ATP) and a moderate red fluorescence signal in Ch 2 ($ONOO^-$). In cells pretreated with SIN-1 (1.0 mM, a commercial $ONOO^-$ donor) for 1 h, the Ch 2 ($ONOO^-$) fluorescence signal significantly increased, while the Ch 1 (ATP) fluorescence signal attenuated. To verify that these changes indeed originated from $ONOO^-$ production, the cells were pretreated with SIN-1 and uric acid (UA, 500 μM, a commercial $ONOO^-$ scavenger) before staining with P2. Fig. 2 showed that the Ch 2 ($ONOO^-$) fluorescence signal was suppressed, while the Ch 1 (ATP) fluorescence signal was restored, suggesting that elevated intracellular $ONOO^-$ levels decrease ATP expression. Oligomycin A (Omy A) was an inhibitor of ATP synthase, and its inhibition occurred in ATP-dependent and oxidative phosphorylation-coupled mitochondrial membrane processes. In comparison to the control group, the cells pretreated with 25 μM Omy A for 1 h elicited a diminished fluorescent signal in Ch 1 (ATP) and an enhanced fluorescent signal in Ch 2 ($ONOO^-$). Correspondingly, when the cells were pretreated with Omy A for 1 h and then added exogenous 10 mM ATP, the Ch 1 (ATP) fluorescence signal significantly intensified, while the Ch 2 ($ONOO^-$) fluorescence signal weakened. This might be attributed to the inhibition of ATP activity by Omy A, which caused mitochondrial dysfunction, resulting in increased $ONOO^-$ levels. These results illustrated that the expression levels of intracellular ATP and $ONOO^-$ interacted with each other and P2 was able to real-time monitor the fluctuation of intracellular ATP and $ONOO^-$ levels.

3.4. Identification of normal and cancer cells

Four cell lines (NP69, CNE1, CNE2, 5–8 F) were chosen to investigate the ability of P2 to differentiate between normal and cancer cells. There was no significant variability in Ch 1 fluorescence intensity among the different cell lines stained with P2. However, Ch 2 fluorescence intensity was lower in normal cells NP69 compared to the cancer cells (CNE1, CNE2, 5–8 F). This indicated that the ATP levels were similar in NP69 and CNE1, CNE2, and 5–8 F cells, whereas the $ONOO^-$ levels exhibited significant differences. As indicated in Fig. 3, merging images clearly displayed the difference in fluorescence imaging between NP69 and CNE1, CNE2, and 5–8 F. The results demonstrated that P2 could identify normal and cancer cells through dual-color fluorescence imaging.

3.5. The interrelationship between ATP and $ONOO^-$ during pyroptosis

AKI represented an inflammatory disease capable of directly impairing vascular endothelial cells through inflammatory responses. During hypoxia-ischemia, the cells were prone to pyroptosis, which accelerated cell death. Previous findings have confirmed that pyroptosis was an essential mode of renal tubular epithelial cell death and loss in the development of AKI from various factors, as well as triggering the onset of the renal inflammatory response [49]. To further elucidate these mechanisms, a chemical hypoxia model using $CoCl_2{\cdot}6\ H_2O$ (an oxygen deprivation reagent) was established. The dual-channel fluorescence signal of P2 was employed to track the level fluctuations of ATP and $ONOO^-$ in cells treated with $CoCl_2{\cdot}6\ H_2O$ (Fig. 4a). Figs. 4b and 4c showed that with increasing $CoCl_2{\cdot}6\ H_2O$ concentration, the Ch 1 fluorescence signal diminished while the Ch 2 fluorescence signal enhanced.

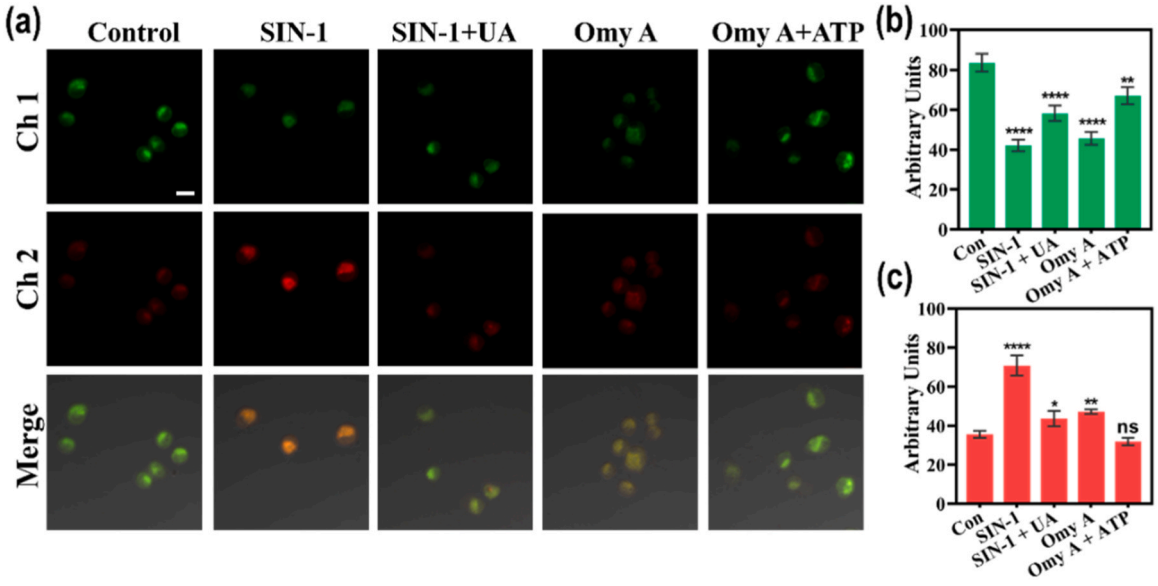

Fig. 2. Fluorescence imaging of ATP and $ONOO^-$ interactions in CNE1 cells. (a) The cells were treated with SIN-1 (1.0 mM), SIN-1 (1.0 mM) and UA (500 μM), Omy A (25 μM), Omy A (25 μM), and ATP (10 mM) for 1.0 h each, respectively, and then stained with P2 (20 μM) for 20 min. (b) Average fluorescence intensity of P2 labeled cells in images A (Ch 1, ATP). (c) Average fluorescence intensity of P2 labeled cells in images (a) (Ch 2, $ONOO^-$). The data were shown as mean ± S.D. (* $P < 0.05$, ** $P < 0.01$, **** $P < 0.0001$, n = 3). Scale bar: 20 μm.

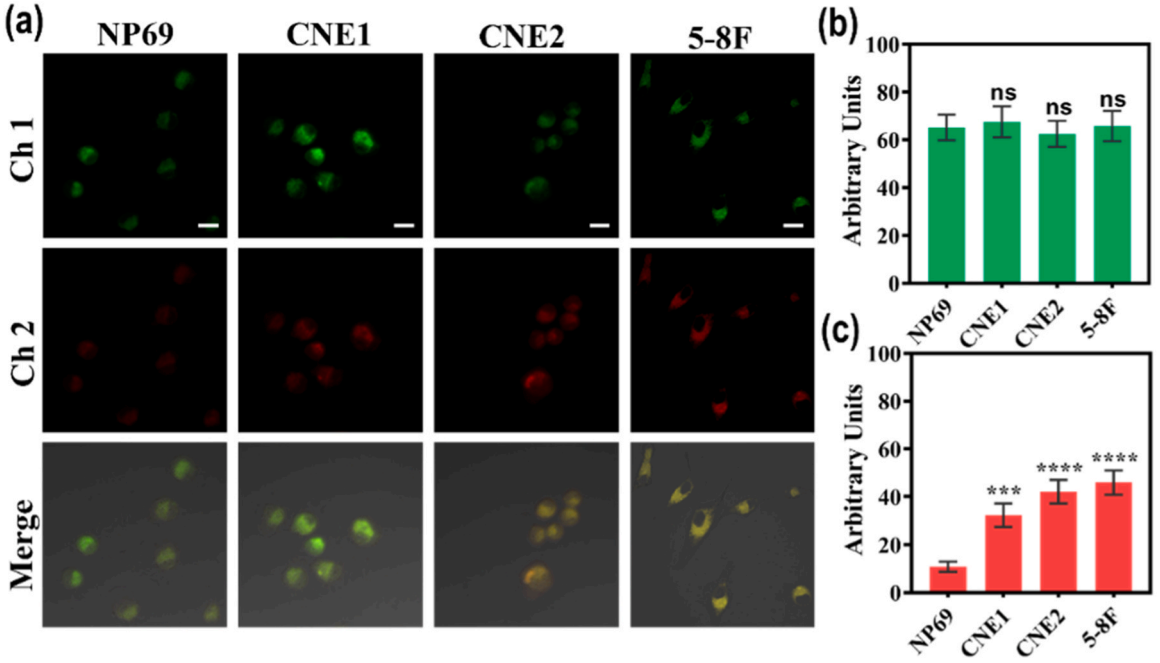

Fig. 3. Fluorescence imaging of ATP and $ONOO^-$ in normal and cancer cells. (a) NP69, CNE1, CNE2, and 5–8 F cells were incubated with P2 (20 μM) for 20 min. (b) Average fluorescence intensity of P2 labeled cells in images (a) (Ch 1, ATP). (c) Average fluorescence intensity of P2 labeled cells in images (a) (Ch 2, $ONOO^-$). The data were shown as mean ± S.D. (*** $P < 0.001$, **** $P < 0.0001$, n = 3). Scale bar: 20 μm.

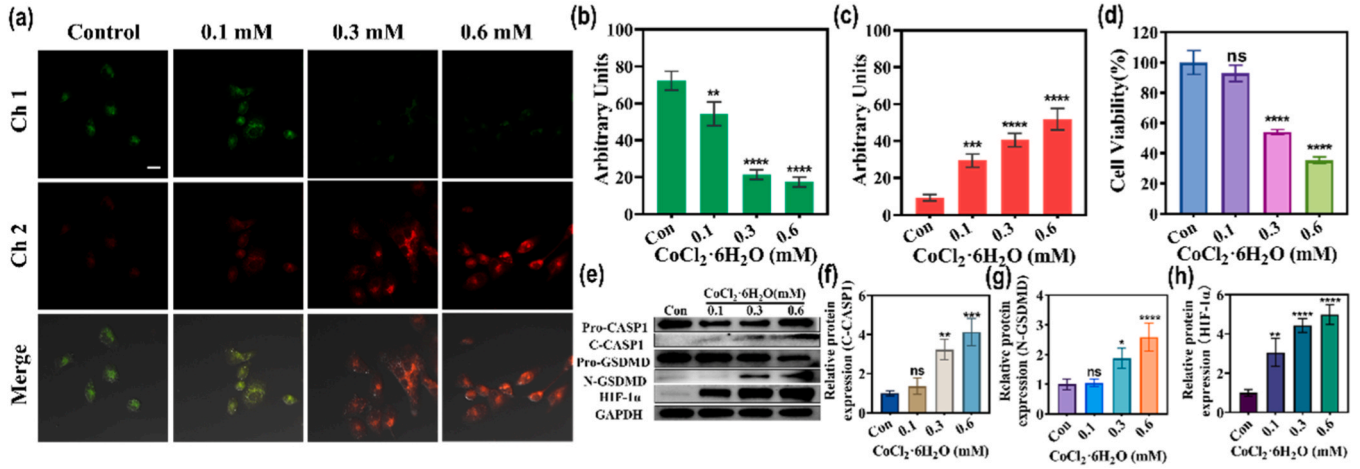

Fig. 4. Oxygen deprivation-induced pyroptosis of HK-2 cells. (a) The cells were pretreated with different concentrations of $CoCl_2{\cdot}6\ H_2O$ (0.1 mM, 0.3 mM, 0.6 mM) for 24 h, and then stained with P2 (20 μM) for 20 min. (b) Average fluorescence intensity of P2 labeled cells in images (a) (Ch 1, ATP). (c) Average fluorescence intensity of P2 labeled cells in images (a) (Ch 2, $ONOO^-$). (d) Cell viability of HK-2 cells upon treatment with different concentrations of $CoCl_2{\cdot}6\ H_2O$ for 24 h. (e) Various concentrations of $CoCl_2{\cdot}6\ H_2O$ pretreated HK-2 cells for 24 h induced the protein levels of C-caspase 1, N-GSDMD, and HIF-1α. (f - h) Relative expression of C-caspase 1, N-GSDMD, and HIF-1α proteins in HK-2 cells pretreated with different concentrations of $CoCl_2{\cdot}6\ H_2O$ for 24 h. The data were shown as mean ± S.D. (* $P < 0.05$, ** $P < 0.01$, *** $P < 0.001$, **** $P < 0.0001$, n = 3). Scale bar: 20 μm.

This indicated that a reduction in intracellular ATP levels was accompanied by a rise in $ONOO^-$ levels. Fig. 4d illustrated that the survival rate of HK-2 cells gradually decreased, directly validating that hypoxia would lead to the deterioration of cell status and even death. To investigate whether HK-2 cells underwent pyroptosis in $CoCl_2{\cdot}6\ H_2O$-induced chemical hypoxia, the expression levels of intracellular pyroptosis-related proteins were further analyzed using western blot. The protein expression level of hypoxia-inducible factor-1α (HIF-1α) significantly increased, proving that $CoCl_2{\cdot}6\ H_2O$ successfully induced hypoxia in HK-2 cells (Figs. 4e, 4h). Compared to the control group, the expression levels of caspase-1 and N-GSDMD proteins were upregulated with increasing concentrations of $CoCl_2{\cdot}6\ H_2O$, suggesting C-caspase 1 was activated to cleave GSDMD, forming N-GSDMD peptide fragments and inducing pyroptosis via the classical caspases-1 dependent pathway (Fig. 4e-g).

Ischemia/hypoxia (I/H) played an important role in the progression of AKI. To reveal whether pyroptosis occurred during I/H and changed the levels of ATP/$ONOO^-$, we further simulated an I/H model using HK-2 cells through oxygen-glucose deprivation. HK-2 cells were switched to sugar-free and serum-free medium and incubated in 95 % N_2, 5 % CO_2 incubator at 37°C for either 1 h or 2 h, then returned to complete medium and continued to incubate for an additional 24 h for subsequent assays. As depicted in Fig. 5a-c, after 1 h of I/H, both Ch 1 (ATP) and Ch 2 ($ONOO^-$) fluorescence signals showed varying degrees of enhancement

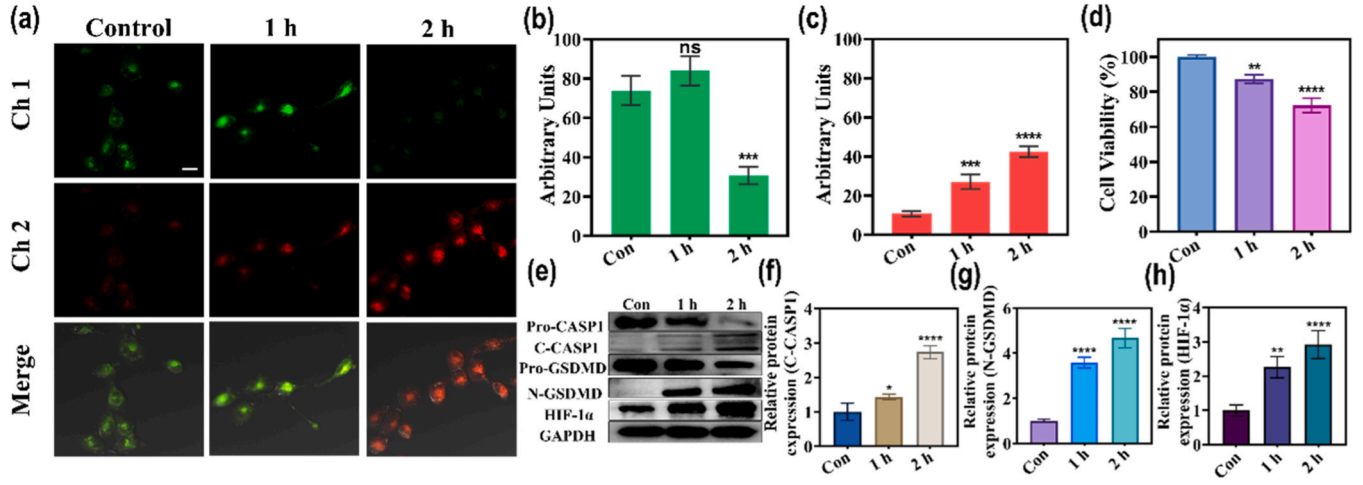

Fig. 5. Oxygen-glucose deprivation-induced pyroptosis of HK-2 cells. (a) The cells treated with oxygen-glucose deprivation for different times (1 h, 2 h) were then stained with P2 (20 μM) for 20 min. (b) Average fluorescence intensity of P2 labeled cells in images (a) (Ch 1, ATP). (c) Average fluorescence intensity of P2 labeled cells in images (a) (Ch 2, $ONOO^-$). (d) Cell viability of HK-2 cells under different times of oxygen-glucose deprivation. (e) Different oxygen-glucose deprivation times induced protein levels of C-caspase 1, N-GSDMD, and HIF-1α in HK-2 cells. (f - h) Relative expression of C-caspase 1, N-GSDMD, and HIF-1α proteins in HK-2 cells under various oxygen-glucose deprivation times. The data were shown as mean ± S.D. (* $P < 0.05$, ** $P < 0.01$, *** $P < 0.001$, **** $P < 0.0001$, n = 3). Scale bar: 20 μm.

compared with the control. Upon 2 h of I/H, the Ch 1 (ATP) fluorescence signal was significantly weakened, and the Ch 2 ($ONOO^-$) fluorescence signal continued to increase. The above phenomena were indicative of a compensatory cellular appearance with enhanced intracellular energy metabolism to resist I/H under a milder degree of I/H. Additionally, we examined the cell viability post-I/H and observed a decrease in cell viability with prolonged I/H duration (Fig. 5d). This suggested that I/H resulted in irreversible cellular damage despite the initial compensatory mechanisms. To demonstrate that HK-2 cells underwent pyroptosis post-I/H, the expression levels of pyroptosis-related proteins were examined. The significant elevation of the HIF-1α protein expression level represented the successful construction of the I/H HK-2 cell model (Figs. 5e, 5h). Western-blot assay revealed the elevated expression levels of C-caspase 1 and N-GSDMD protein, supporting the activation of caspase 1, cleavage of GSDMD, and induction of pyroptosis under acute I/H condition (Fig. 5e-g).

3.6. Protective effect of UA on HK-2 cells post-I/H

The findings in Fig. 5 testified that I/H HK-2 cells underwent pyroptosis, concomitant with decreased intracellular ATP and increased $ONOO^-$. UA was a commercial selective $ONOO^-$ scavenger that effectively inhibited $ONOO^-$-mediated cellular damage. The protective effect of UA on I/H HK-2 cells was then investigated. As seen in Fig. 6a-c, the fluorescence signal of Ch 1 (ATP) was enhanced in the UA-treated group (2 h + UA) compared to the I/H group (2 h + DMSO), while the fluorescence signal of Ch 2 ($ONOO^-$) was reduced, meaning UA effectively cleared the excessive $ONOO^-$ production within cells. The significant

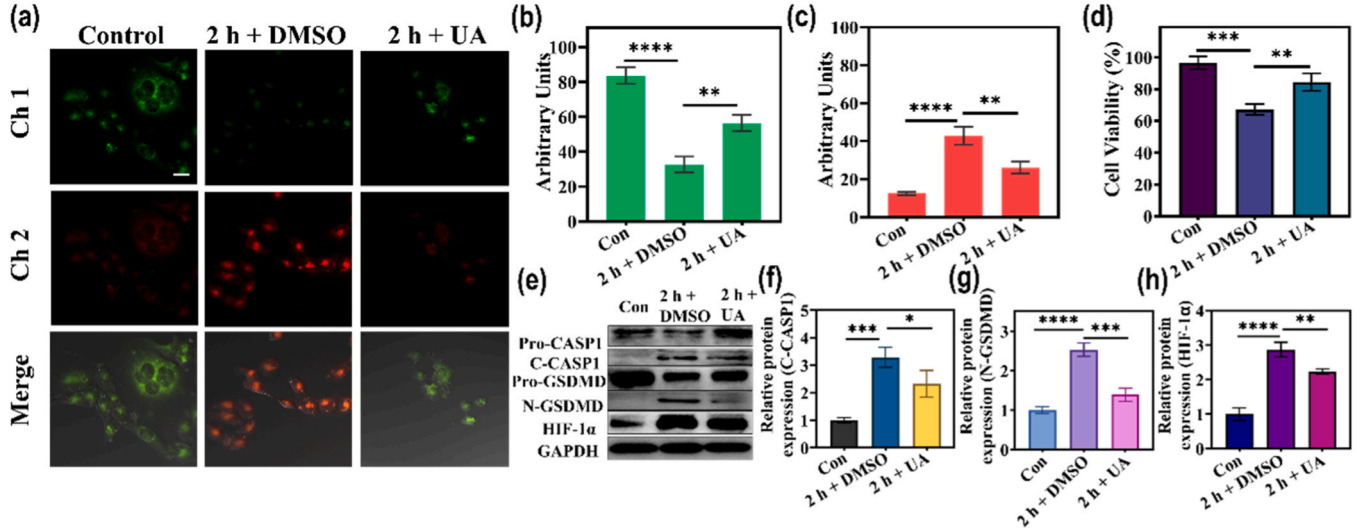

Fig. 6. Protective effect of UA on HK-2 cells post-I/H. Control group: no treatment; 2 h + DMSO: 2 h of I/H while adding 5 μL of DMSO per ml of the medium; 2 h + UA: 2 h of I/H with simultaneous addition of UA (500 μM). (a) The cells treated with oxygen-glucose deprivation for different times (1 h, 2 h) were then stained with P2 (20 μM) for 20 min. (b) Average fluorescence intensity of P2 labeled cells in images (a) (Ch 1, ATP). (c) Average fluorescence intensity of P2 labeled cells in images (a) (Ch 2, $ONOO^-$). (d) Cell viability of HK-2 cells under 2 h + DMSO, 2 h + UA treatments. (e) 2 h + DMSO, 2 h + UA induced protein levels of C-caspase 1, N-GSDMD, and HIF-1α in HK-2 cells. (f - h) Relative expression of C-caspase 1, N-GSDMD, and HIF-1α proteins in HK-2 cells under 2 h + DMSO, 2 h + UA treatments. The data were shown as mean ± S.D. (* $P < 0.05$, ** $P < 0.01$, *** $P < 0.001$, **** $P < 0.0001$, n = 3). Scale bar: 20 μm.

increase in cell survival in the UA-treated group, demonstrated in Fig. 6d, further supported the protective role of UA against I/H-induced cellular damage. We also explored whether UA protected HK-2 cells from injury by inhibiting the pyroptosis pathway. Western-blot analysis revealed that the addition of UA to cells resulted in decreased activation of C-caspase-1 and cleaved N-GSDMD, along with a reduction in the downregulation of HIF-1α protein (Fig. 6e-h). The above protein level assays signified UA could improve the hypoxic condition of HK-2 cells and attenuate cellular injury by reducing I/H-induced pyroptosis through inhibition of the caspase 1-dependent classical pathway. These results indicated UA could be used as a potential inhibitor of pyroptosis, providing a therapeutic strategy for protecting cells from I/H-induced damage.

3.7. *In vivo visualization of ATP and ONOO⁻ activity in AKI mice*

Encouraged by the excellent imaging capabilities of P2 at the cellular level, we extended its application to visualize ATP and ONOO⁻ activity in AKI mice. C57BL/6 mice were deeply anesthetized, and the left kidney tip was clamped for 15 min and then released for reperfusion. The right kidney served as an untreated group. The kidneys were injected *in situ* with P2 at 24 h, 48 h, and 72 h post-injury and imaged 30 min later. In Ch 1 (ATP), the fluorescence signal of the right kidney hardly changed, whereas the left kidney exhibited an initial decrease followed by a slow rebound in fluorescence signal compared to the right kidney. In Ch 2 (ONOO⁻), minimal fluorescence was observed in the right kidney, while the fluorescence signal in the left kidney was sharply enhanced at 24 h in comparison to the left kidney (Fig. 7a-c). The fluorescence signal of the left kidney in Ch 2 remained high at 72 h but decreased slightly compared with 24 h. The reason might be that part of ONOO⁻ was eliminated through the glomerulus and tubules, down-regulating the intrarenal ONOO⁻ level. The *in vivo* imaging results implied the kidneys produced large amounts of ONOO⁻ and experienced rapid ATP depletion within 24 h of acute ischemia-reperfusion (I/R). With the extension of reperfusion time to 72 h, certain undamaged cells in the left kidney compensated for the intracellular activities and energy metabolism to restore the intrarenal ATP level to normal. After 72 h, the kidney tissues were cut into sections of 10 μm thickness for H&E staining (Fig. 7d, e). The normal right kidney tissues visualized clear renal tissue structures, while the ischemic left kidney tissues appeared to have necrotic epithelial cells and mildly dilated renal tubules. H&E staining results corroborated the successful establishment of the AKI mice model. Further, a bilateral mouse model of renal I/R AKI was established on this basis. After 24 h of I/R, the fluorescence signal of Ch 1 (ATP) decreased

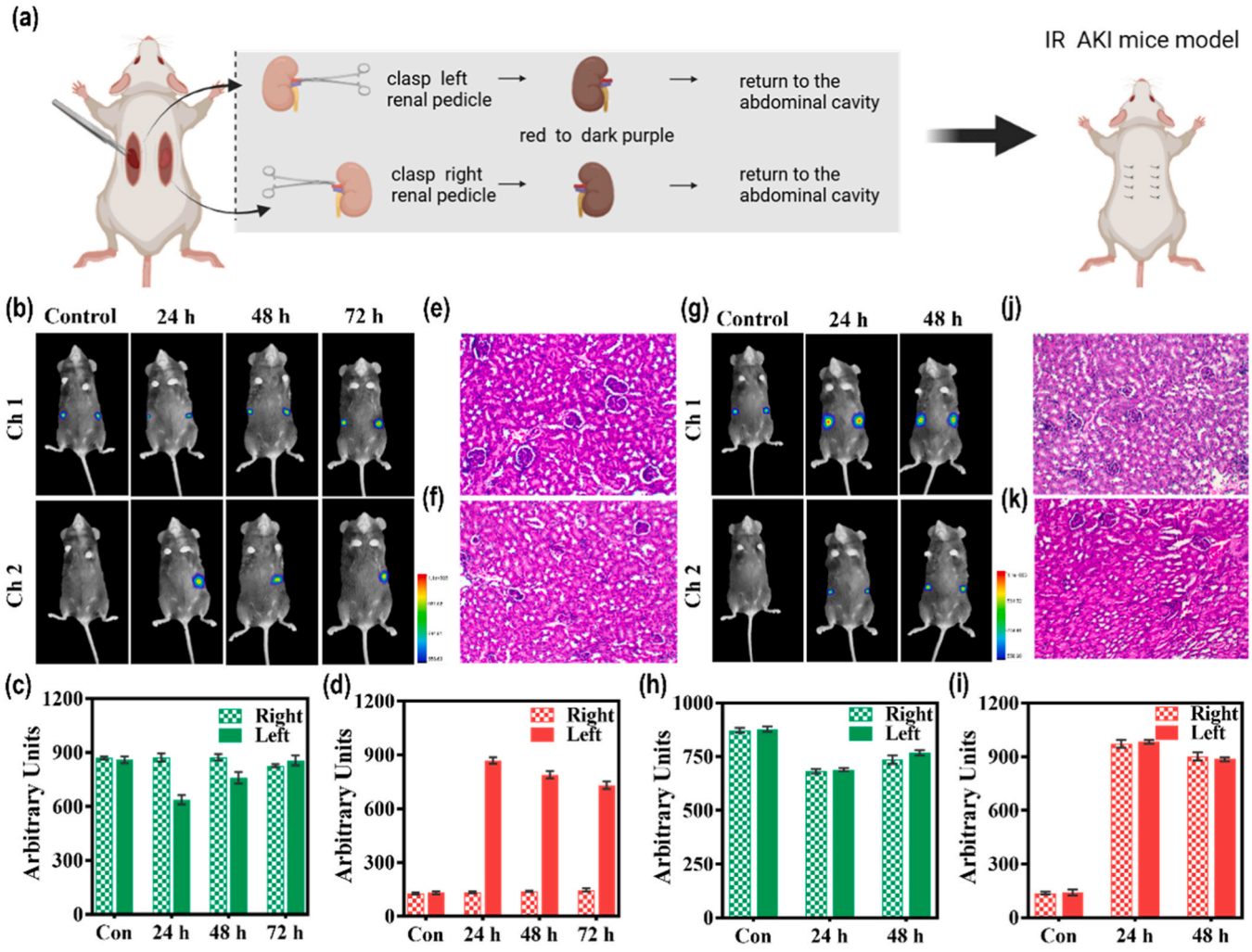

Fig. 7. (a) An illustration of the experiment design for the mice model. (b) Imaging of ATP and ONOO⁻ in the kidney of unilateral ischemic AKI mice. Acute ischemia of the left kidney for 15 min followed by reperfusion for 24 h, 48 h, 72 h; no treatment of the right kidney. (c) Average fluorescence intensity of Ch 1 images in panel (b). (d) Average fluorescence intensity of Ch 2 images in panel (b). (e, f) H&E staining results of the left and right kidneys (72 h of reperfusion). (g) Imaging of ATP and ONOO⁻ in the kidney of bilateral ischemic AKI mice. Acute ischemia of the right and left kidney for 15 min followed by reperfusion for 24 h and 48 h. (h) Average fluorescence intensity of Ch 1 images in panel (g). (i) Average fluorescence intensity of Ch 2 images in panel (g). The data were shown as mean ± S.D. (n = 3). (j, k) H&E staining results of the left and right kidneys, respectively. The illustration (a) was created with the help of BioRender.com.

in both left and right kidneys, returning to near-normal levels at 48 h (Figs. 7f, 7g). The fluorescence signal of Ch 2 ($ONOO^-$) significantly increased at 24 h of I/R and slightly decreased at 48 h in both kidneys (Figs. 7f, 7h). H&E sections of both bilateral ischemic tissues displayed massive epithelial cell necrosis, degeneration, and moderate to severe renal tubular dilatation (Figs. 7i, 7j). Upon bilateral acute I/R, a large amount of $ONOO^-$ was generated, resulting in a rapid depletion of ATP. These findings illustrated that P2 was capable of detecting and visualizing ATP and $ONOO^-$ *in vivo*, as well as its capability to distinguish the severity of AKI.

4. Conclusion

In summary, we have disclosed a novel NIRF probe P2 with dual-color fluorescence emission and harnessed it for the simultaneous detection of ATP and $ONOO^-$ *in vitro* and *in vivo*. P2 possessed outstanding optical properties for imaging intracellularly endogenous and exogenous ATP and $ONOO^-$ and distinguishes between cancerous and normal cells. The research unveiled an interplay between ATP and $ONOO^-$, with an imbalance closely related to pyroptosis and AKI. Utilizing the dual-color imaging capability of P2, the dynamics of ATP and $ONOO^-$ during pyroptosis were sensitively monitored. In the $CoCl_2{\cdot}6\ H_2O$ and oxygen-glucose deprivation-stimulated HK-2 cell experiments, not only did WB analysis reveal that cellular pyroptosis was triggered via the caspase-1-dependent classical pathway, but also a significant increase in the level of $ONOO^-$ and a decrease in the level of ATP were observed. Moreover, UA was found to have a prominent cytoprotective effect, suggesting its potential as a therapeutic agent through the inhibition of pyroptosis. Benefitting from P2, we successfully tracked changes in ATP and $ONOO^-$ levels in the AKI mice model. Specifically, $ONOO^-$ levels were dramatically elevated in the kidneys of AKI mice, while ATP levels initially declined and then gradually recovered with the prolongation of reperfusion time. These findings further demonstrated the detection and diagnostic potential of P2 in the process of AKI. We believed that an in-depth exploration of ATP and $ONOO^-$ interactions would offer valuable insights into the development of innovative diagnostic and therapeutic approaches for related diseases.

CRediT authorship contribution statement

Xuejun Zhou: Resources. **Xiaofeng Wang:** Conceptualization. **Xuan Liu:** Formal analysis. **Yiying Li:** Funding acquisition. **Heng Liu:** Writing – review & editing, Supervision, Resources, Project administration, Methodology, Funding acquisition. **Fabiao Yu:** Writing – review & editing, Funding acquisition, Conceptualization. **Yan Wang:** Writing – review & editing, Formal analysis. **Qing Ye:** Funding acquisition, Conceptualization. **Yuxia Zou:** Writing – original draft, Data curation, Conceptualization. **Tingting Duan:** Validation, Methodology.

Declaration of Competing Interest

The authors declare that they have no known competing financial interests or personal relationships that could have appeared to influence the work reported in this paper.

Data availability

Data will be made available on request.

Acknowledgements

This work was supported by the National Natural Science Foundation of China (22264013), Natural Science Foundation of Fujian Province (2020J011104), Fujian Provincial Health Technology Project (2021GGA004), Special Funds of S&T Cooperation and Exchange Projects of Shanxi Province (202204041101040), Hainan Province Science and Technology Special Fund (ZDYF2021SHFZ219, ZDYF2022SHFZ037), Hainan Provincial Natural Science Foundation of China (822RC831, 821QN260), Natural Science Research Talent Project of Hainan Medical University (JBGS202101), Project of Hainan Association for Science and Technology of Youth Science and Talents (QCXM202023), Project for Functional Materials and Molecular Imaging Science Innovation Group of Hainan Medical University and Hainan Province Clinical Medical Center (2021). Thanks to the support and assistance in terms of instruments and facilities provided by Public Research Center of Hainan Medical University.

Appendix A. Supporting information

Supplementary data associated with this article can be found in the online version at doi:10.1016/j.snb.2024.136367.

References

[1] F. Schütt, S. Aretz, G.U. Auffarth, J. Kopitz, Moderately reduced atp levels promote oxidative stress and debilitate autophagic and phagocytic capacities in human RPE cells, Invest. Ophthalmol. Vis. Sci. 53 (2012) 5354–5361.
[2] B. Terni, J. Boada, M. Portero-Otin, R. Pamplona, I. Ferrer, Mitochondrial ATP-synthase in the entorhinal cortex is a target of oxidative stress at stages i/ii of Alzheimer's disease pathology, Brain. Pathol. 20 (2010) 222–233.
[3] C.M. Cruz, A. Rinna, H.J. Forman, A.L. Ventura, P.M. Persechini, D.M. Ojcius, ATP activates a reactive oxygen species-dependent oxidative stress response and secretion of proinflammatory cytokines in macrophages, J. Biol. Chem. 282 (2007) 2871–2879.
[4] J. Dan Dunn, L.A. Alvarez, X. Zhang, T. Soldati, Reactive oxygen species and mitochondria: a nexus of cellular homeostasis, Redox Biol. 6 (2015) 472–485.
[5] M. Mittal, M.R. Siddiqui, K. Tran, S.P. Reddy, A.B. Malik, Reactive oxygen species in inflammation and tissue injury, Antioxid. Redox Signal. 20 (2014) 1126–1167.
[6] P. Yu, X. Zhang, N. Liu, L. Tang, C. Peng, X. Chen, Pyroptosis: mechanisms and diseases, Signal. Transduct. Target 6 (2021) 128.
[7] T. Bergsbaken, S.L. Fink, B.T. Cookson, Pyroptosis: Host cell death and inflammation, Nat. Rev. Microbiol. 7 (2009) 99–109.
[8] X. Xia, X. Wang, Z. Cheng, W. Qin, L. Lei, J. Jiang, et al., The role of pyroptosis in cancer: pro-cancer or pro-"host"? Cell. Death. Dis. 10 (2019), 650.
[9] Y.J. Xu, L. Zheng, Y.W. Hu, Q. Wang, Pyroptosis and its relationship to atherosclerosis, Clin. Chim. Acta 476 (2018) 28–37.
[10] S.B. Kovacs, E.A. Miao, Gasdermins: effectors of pyroptosis, Trends Cell. Biol. 27 (2017) 673–684.
[11] B.A. McKenzie, V.M. Dixit, C. Power, Fiery cell death: pyroptosis in the central nervous system, Trends Neurosci. 43 (2020) 55–73.
[12] Z. Zhaolin, L. Guohua, W. Shiyuan, W. Zuo, Role of pyroptosis in cardiovascular disease, Cell. Prolif. 52 (2019) e12563.
[13] Q.B. Zha, H.X. Wei, C.G. Li, Y.D. Liang, L.H. Xu, W.J. Bai, et al., ATP-induced inflammasome activation and pyroptosis is regulated by AMP-activated protein kinase in macrophages, Front. Immunol. 7 (2016) 597.
[14] Y. Wang, Y. Li, Y. Xu, Pyroptosis in kidney disease, J. Mol. Biol. 434 (2022) 167290.
[15] N. Li, Y. Wang, X. Wang, N. Sun, Y.H. Gong, Pathway network of pyroptosis and its potential inhibitors in acute kidney injury, Pharmacol. Res. 175 (2022) 106033.
[16] W. Xia, Y. Li, M. Wu, Q. Jin, Q. Wang, S. Li, et al., Gasdermin E deficiency attenuates acute kidney injury by inhibiting pyroptosis and inflammation, Cell. Death. Dis. 12 (2021) 139.
[17] J.A. Kellum, P. Romagnani, G. Ashuntantang, C. Ronco, A. Zarbock, H.-J. Anders, Acute kidney injury, Nat. Rev. Dis. Prim. 7 (2021) 52.
[18] C. Ronco, R. Bellomo, J.A. Kellum, Acute kidney injury, Lancet 394 (2019) 1949–1964.
[19] C.P.C. Ow, A. Trask-Marino, A.H. Betrie, R.G. Evans, C.N. May, Y.R. Lankadeva, Targeting oxidative stress in septic acute kidney injury: from theory to practice, J. Clin. Med. 10 (2021).
[20] J.A. Funk, R.G. Schnellmann, Persistent disruption of mitochondrial homeostasis after acute kidney injury, Am. J. Physiol. -Ren. Physiol. 302 (2012) F853–F864.
[21] A.A. Sharfuddin, B.A. Molitoris, Pathophysiology of ischemic acute kidney injury, Nat. Rev. Nephrol. 7 (2011), 189-200.
[22] J.D. Bauerle, A. Grenz, J.-H. Kim, H.T. Lee, H.K. Eltzschig, Adenosine generation and signaling during acute kidney injury, J. Am. Soc. Nephrol. 22 (2011) 14–20.
[23] S.H. Su, S.J. Su, L.Y. Huang, Y.C. Chiang, Leukemic cells resist lysosomal inhibition through the mitochondria-dependent reduction of intracellular pH and oxidants, Free. Radic. Biol. Med. 198 (2023) 1–11.
[24] H. Wang, J. Liu, L. Wu, Methylglyoxal-induced mitochondrial dysfunction in vascular smooth muscle cells, Biochem. Pharmacol. 77 (2009) 1709–1716.
[25] J. Huang, J. Li, Y. Lyu, Q. Miao, K. Pu, Molecular optical imaging probes for early diagnosis of drug-induced acute kidney injury, Nat. Mater. 18 (2019) 1133–1143.
[26] L. He, H. Liu, J. Wu, Z. Cheng, F. Yu, Construction of a mitochondria-endoplasmic reticulum dual-targeted red-emitting fluorescent probe for imaging peroxynitrite in living cells and zebrafish, Chem. Asian J. 17 (2022) e202200388.

[27] L. Xiao, X. Sun, Z. Li, Y. Zhang, P. Zhang, Y. He, et al., Recent progress in rational design of peroxynitrite fluorescent probes and bioapplication, Dyes Pigments 216 (2023) 111385.
[28] J. Sun, X. Cao, W. Lu, Y. Wei, L. Kong, W. Chen, et al., Recent advances in fluorescent probes of peroxynitrite: structural, strategies and biological applications, Theranostics 13 (2023) 1716–1744.
[29] M. Ren, C. Zhou, L. Wang, X. Lv, W. Guo, Rationally designed meso-benzimidazole-pyronin with emission wavelength beyond 700 nm enabling in vivo visualization of acute-liver-injury-induced peroxynitrite, Chin. Chem. Lett. 34 (2023) 107646.
[30] M. Domínguez, K. Meyer, F. Sancenón, J.F. Blandez, M. Serrano, R. Martínez-Máñez, A. NIR, fluorescent probe for the detection of renal damage based on overrepresentation of alanine aminopeptidase enzyme, Chem. Commun. 59 (2023) 2481–2484.
[31] J. Lu, K. Dou, Z. Geng, Z. Wang, Construction of near-infrared ratiometric fluorescent probes with emission crosstalk-free for reversible atp tracking in mitochondria and tumors, Sens. Actuators B Chem. 390 (2023) 134043.
[32] M. Li, P. Lei, S. Shuang, C. Dong, L. Zhang, Recent advances in fluorescent probes for dual-detecting $ONOO^-$ and analytes, Spectrochim. Acta A 303 (2023) 123179.
[33] Y. Ji, S. Liu, J. Zhang, L. Qu, J. Wu, H. Liu, et al., Construction of HPQ-based activatable fluorescent probe for peroxynitrite and its application in ferroptosis and mice model of LPS-induced inflammation, Bioorg. Chem. 138 (2023) 106650.
[34] W.L. Cui, M.H. Wang, Y.H. Yang, J.Y. Wang, X. Zhu, H. Zhang, et al., Recent advances and perspectives in reaction-based fluorescent probes for imaging peroxynitrite in biological systems, Coord. Chem. Rev. 474 (2023) 214848.
[35] W. Qu, C. Niu, X. Zhang, W. Chen, F. Yu, H. Liu, et al., Construction of a novel far-red fluorescence light-up probe for visualizing intracellular peroxynitrite, Talanta 197 (2019) 431–435.
[36] X. Chai, B. Li, C. Chen, W. Zhang, L. Sun, H.H. Han, et al., A highly sensitive and selective near-infrared fluorescent probe for imaging peroxynitrite in living cells and drug-induced liver injury mice, Anal. Chem. 95 (2023) 5747–5753.
[37] H. Zhang, Y. Xu, H. Li, W. Shi, X. Li, H. Ma, New rhodamines with changeable π-conjugation for lengthening fluorescence wavelengths and imaging peroxynitrite, Chem 8 (2022) 287–295.
[38] P. Wang, L. Yu, J. Gong, J. Xiong, S. Zi, H. Xie, et al., An activity-based fluorescent probe for imaging fluctuations of peroxynitrite ($ONOO^-$) in the Alzheimer's disease brain, Angew. Chem. Int. Ed. 61 (2022) e202206894.
[39] M.P. Murphy, H. Bayir, V. Belousov, C.J. Chang, K.J.A. Davies, M.J. Davies, et al., Guidelines for measuring reactive oxygen species and oxidative damage in cells and in vivo, Nat. Metab. 4 (2022) 651–662.
[40] W.L. Jiang, W.X. Wang, Z.Q. Wang, M. Tan, G.J. Mao, Y. Li, et al., A tumor-targeting near-infrared fluorescent probe for real-time imaging ATP in cancer cells and mice, Anal. Chim. Acta 1206 (2022) 339798.
[41] W. Yang, R. Liu, X. Yin, Y. Jin, L. Wang, M. Dong, et al., Peroxynitrite activated near-infrared fluorescent probe for evaluating ferroptosis-mediated acute kidney injury, Sens. Actuators B Chem. 393 (2023) 134180.
[42] B. Huang, B. Liang, R. Zhang, D. Xing, Molecule fluorescent probes for adenosine triphosphate imaging in cancer cells and in vivo, Coord. Chem. Rev. 452 (2022) 214302.
[43] Z. Tang, B. Song, W. Zhang, L. Guo, J. Yuan, Precise monitoring of drug-induced kidney injury using an endoplasmic reticulum-targetable ratiometric time-gated luminescence probe for superoxide anions, Anal. Chem. 91 (2019) 14019–14028.
[44] L. Wu, J. Liu, X. Tian, R.R. Groleau, B. Feng, Y. Yang, et al., Dual-channel fluorescent probe for the simultaneous monitoring of peroxynitrite and adenosine-5′-triphosphate in cellular applications, J. Am. Chem. Soc. 144 (2022) 174–183.
[45] W. Zhang, Y. Lv, F. Huo, Y. Zhang, C. Yin, Dual-site fluorescent probe for bioimaging of upregulated adenosine triphosphate under the stresses of endogenous and exogenous H_2S, Dyes Pigments 204 (2022) 110442.
[46] X. Yang, P. Xie, J. Liu, X. Han, D. Zhang, Y. Ye, et al., Dual-site fluorescent sensor for tracking lysosomal atp and H_2S during liver injury, Chem. Eng. J. 442 (2022) 136141.
[47] P. Sun, H.C. Chen, S. Lu, J. Hai, W. Guo, Y.H. Jing, et al., Simultaneous sensing of H_2S and ATP with a two-photon fluorescent probe in Alzheimer's disease: toward understanding why H_2S regulates glutamate-induced atp dysregulation, Anal. Chem. 94 (2022) 11573–11581.
[48] Y. Fang, W. Shi, Y. Hu, X. Li, H. Ma, A dual-function fluorescent probe for monitoring the degrees of hypoxia in living cells via the imaging of nitroreductase and adenosine triphosphate, Chem. Commun. 54 (2018) 5454–5457.
[49] E.E. Elias, B. Lyons, D.A. Muruve, Gasdermins and pyroptosis in the kidney, Nat. Rev. Nephrol. 19 (2023) 337–350.

Yuxia Zou is an attending doctor at the Department of Otolaryngology, Head and Neck Surgery, the First Affiliated Hospital of Hainan Medical University. His research interests focus on optical diagnosis.

Tingting Duan is an attending doctor at the First Affiliated Hospital of Hainan Medical University. His research interests focus on optical diagnosis.

Yan Wang is a master's degree student at Shengli Clinical Medical College of Fujian Medical University.

Qing Ye is a senior doctor at Shengli Clinical Medical College of Fujian Medical University, Department of Otolaryngology, Head and Neck Surgery, Fujian Provincial Hospital. His research interests focus on the diagnosis and treatment of otolaryngology-related diseases.

Yiying Li is a lecturer at Hainan Medical University. His research interests focus on neuropharmacology and cardiovascular pharmacology.

Xiaofeng Wang is a senior doctor at the First Affiliated Hospital of Hainan Medical University. He received his Ph.D. degree from Xinjiang Medical University in 2006. His research interests focus on the diagnosis and treatment of otolaryngology-related diseases.

Xuan Liu is a master's degree student at the First Affiliated Hospital of Hainan Medical University.

Xuejun Zhou is a senior doctor at the First Affiliated Hospital of Hainan Medical University. He received his Ph.D. degree from Xinjiang Medical University in 2006. His research interests focus on the diagnosis and treatment of otolaryngology-related diseases.

Fabiao Yu is a professor at Hainan Medical University. His research interests focus on molecular diagnosis of tropical disease, multi-modal visual surgery navigation, and point-of-care testing (POCT) technology.

Heng Liu is a professor at Hainan Medical University since 2020. He received his Ph.D. degree from the University of Chinese Academy of Sciences in 2014. His research interests included the development of fluorescent probes and advanced molecular imaging agents.